Depuccio, DP.; Ruiz-Rodríguez, L.; Rodriguez-Castellon, E.; Botella Asuncion, P.; López Nieto, JM.; Landry, CC. (2016). Investigating the Influence of Au Nanoparticles on Porous SiO2-WO3 and WO3 Methanol Transformation Catalysts. Journal of Physical Chemistry C. 120(49):27954-27963. doi:10.1021/acs.jpcc.6b08125.

Investigating the Influence of Au Nanoparticles on Porous SiO_2-WO_3 and WO_3 Methanol Transformation Catalysts

*Daniel P. DePuccio,[a] Lidia Ruíz-Rodríguez,[b] Enrique Rodríguez-Castellón,[c] Pablo Botella,[b] José M. López Nieto,[b] and Christopher C. Landry [a]**

[a] *Department of Chemistry, University of Vermont*
82 University Place, Burlington, VT 05405, USA
[b] *Instituto de Tecnología Química, UPV-CSIC*
Universitat Politècnica de València-Consejo Superior de Investigaciones Científicas,
Avenida de los Naranjos s/n, 46022 Valencia, Spain
[c] *Dpto. Química Inorgánica, Facultad de Ciencias, Universidad de Málaga, 29071 Málaga, Spain*

*To whom correspondence should be addressed. E-mail: christopher.landry@uvm.edu. Fax: +1 802 656 8705.

Abstract

Analyzing the structural and chemical properties of materials at the interface of metal nanoparticles and metal oxide supports is important for catalytic applications. Tungsten oxide (WO_3) is a widely studied catalyst, but changing the catalytic reactivity at the surface of this oxide with metal nanoparticles is of interest. In this work, we sought to modify the redox properties of porous WO_3 and SiO_2-WO_3 catalysts with sonochemically deposited gold nanoparticles (Au NPs) in order to access and study this reaction pathway. Characterization using powder X-ray diffraction (XRD), high-resolution transmission electron microscopy (HR-TEM), X-ray photoelectron spectroscopy (XPS), and inductively-coupled plasma optical emission spectroscopy (ICP-OES) confirmed that crystalline Au NPs with diameters of 5 – 12 nm were distributed throughout the catalysts. Temperature-programmed desorption (TPD) was used to probe the surface acidity of the catalysts. The physic-chemical characteristics of catalysts have been also discussed by considering the catalytic performance of these materials in the aerobic transformation of methanol. Catalysts containing nanocrystalline WO_3 but no Au NPs displayed very high selectivity to DME (> 60%) at all conversions with minor oxidation reactivity, which highlighted the acidic nature of these catalysts. No effect on the acidity of the catalysts was observed by TPD when Au NPs were loaded in the catalysts. The reducibility of the crystalline WO_3 species, however, increased significantly due to the interaction with Au NPs, as observed by temperature-programmed reduction (TPR). In the gas-phase transformation of MeOH under aerobic conditions, catalysts modified with Au NPs showed greater activity compared to non-modified catalysts. In addition, oxidation selectivity to products such as methyl formate as well as formaldehyde, dimethoxymethane, and carbon oxides became heavily favored with only minor dehydration selectivity. The redox properties of these WO_3 catalysts could be tuned by changing the Au loading. More labile lattice oxygen and enhanced redox properties at the surface of WO_3 modified with Au NPs clearly altered these traditional dehydration catalysts to potential oxidation catalysts. Thus, modification of WO_3 with Au is an effective way to expand the MeOH transformation product distribution beyond DME to other useful, oxidized products not typically observed over pure WO_3.

Keywords: tungsten oxide, gold nanoparticles, methanol, oxidation, dehydration, TPR, redox

Introduction

Supported tungsten oxide (WO_3) materials are highly efficient dehydration catalysts, and they have been mainly studied as dispersed monomers, oligomers, and clusters on various supports.[1-11] These previous studies have established a good understanding of the performance of these catalysts as a function of WO_3 domain size and support effects. The acid site reactivity of WO_3 catalysts is commonly probed using the selective transformation of methanol (MeOH) to dimethyl ether (DME).[12] Unlike dispersed WO_3 catalysts, crystalline nanoparticles of WO_3 have received little attention as an acid catalyst.[13,14] The bulk particles behave similarly to their dispersed counterparts, with dehydration serving as the major reaction pathway. The MeOH dehydration reaction to yield DME is very appealing due to the potential widespread use of DME as an alternative fuel to help meet our future energy needs.[15-18] Industrially, this reaction is usually carried out over γ-Al_2O_3 or zeolites such as ZSM-5,[19,20] which possess strong acid sites that are prone to rapid deactivation. Weaker acid sites on WO_3 are expected to have lower rates of deactivation at the expense of lower activities compared to these industrial catalysts.[16] Some studies suggest, however, that crystalline WO_3 catalysts may perform better than WO_3 dispersed on MCM-41 in the dehydration of 1-butanol.[14]

In addition, selective oxidations are also desirable over transition metal oxide catalysts. For example, oxidations of aryl alcohols in the liquid phase have been recently studied with V_2O_5/WO_3 composite catalysts with *tert*-butyl hydrogen peroxide being used as the oxidant.[21] Baeck and coworkers used mixed oxide V_2O_5-WO_3 catalysts in the partial oxidation of ethanol in the gas phase.[22] The highest activity and good selectivity to acetaldehyde were observed when the catalyst composition was 95% V_2O_5 – 5% WO_3. Interestingly, the catalysts containing mostly WO_3 performed the worst. Oxidations of olefins to epoxides are also readily accessible in the presence of WO_3 catalysts and peroxide,[23-26] and semiconducting WO_3 serves as a very efficient catalyst in photochemical and electrochemical oxidation reactions.[27-29]

Despite success in these applications, catalysts containing mostly WO_3 have been limited in gas-phase thermal oxidations of alcohols with O_2 or air as the only oxidant. The poor alcohol oxidation reactivity of pure WO_3 may be attributed to the non-labile lattice oxygen atoms of WO_3 under catalytic conditions that favor dehydration. Once formed, however, oxygen-deficient tungsten oxide (WO_{3-x}) can stabilize various reduced states with differing amounts of oxygen vacancies.[29,30] Recently, DFT calculations and experimental data have shown that reduced tungsten oxides are very active for hydrogenation reactions, and that there is a linear relationship between hydrogenation activity and oxygen vacancy concentration.[30] Therefore, it is expected that increasing the reducibility of WO_3 will increase the reactivity of the surface lattice oxygen species, highlighting an opportunity to use modified WO_3 catalysts for thermal gas-phase oxidations. Blackman and coworkers synthesized Au nanoparticles ("Au NPs") supported on WO_3 nanostructures by using an aerosol assisted chemical vapor deposition (AACVD)

method using a gold-phosphine complex.[31] The catalytic activity of these materials was studied in the solution-phase oxidation of benzyl alcohol to benzaldehyde with *tert*-butyl hydrogen peroxide. Energy-dispersive X-ray spectroscopy and XPS experiments revealed reduced tungsten species in Au-modified WO_3, which explained the increase in catalyst activity compared to pure WO_3 with respect to the entire catalyst (Au and WO_3). However, the selectivity to benzaldehyde was similar for Au-modified WO_3 (100%) and pure WO_3 (94%), which suggests a similar mechanism over both catalysts.

Interactions at the metal nanoparticle – metal oxide interface can have a major influence on the redox properties of a catalyst. Hydrogen temperature-programmed reduction (H_2-TPR) has been used to characterize the reducibility of oxides in the presence of Au NPs. Several studies have analyzed systems such as Au/Fe_2O_3[32] and Au/CeO_2[33-35] using this method, but to the best of our knowledge, the redox behavior of WO_3 in the presence of Au NPs has not been thoroughly explored by H_2-TPR. Gold nanoparticles can weaken metal – oxygen bonds, causing more facile reduction of the oxide. The extent of this effect depends on the preparation method of the Au-oxide catalyst and the concentration of nanoparticles within the oxide.[33,34]

In this study, we sought to explore the reducibility of WO_3 with Au NPs, using the transformation of MeOH as a probe reaction. This reaction serves as a good catalytic characterization tool to better understand acid and redox catalysts. A combined sonochemical and hard-templating method was used to prepare crystalline porous WO_3 catalysts loaded with monodisperse Au NPs to modify the reducibility of WO_3. Several experimental techniques were used to characterize the effects of Au NPs on WO_3 structure and reactivity. The acidic nature of the WO_3 catalysts was confirmed by temperature-programmed desorption (TPD), and differences in WO_3 reducibility were probed by TPR in the presence and absence of deposited Au NPs and the oxidation state of Au was analyzed by XPS. Finally, the gas-phase MeOH transformation reaction was carried out under aerobic conditions with Au-modified and non-modified catalysts. Comparisons between the two types of materials were made to learn more about the role of Au NPs in tuning the activity and redox properties of these WO_3 catalysts.

Experimental

Synthesis of WO_3- and Au- containing catalysts. Porous catalysts containing WO_3 were prepared via a hard-templating technique using ammonium metatungstate as the WO_3 precursor and porous SiO_2 spheres as hard templates. The sonochemical deposition of Au NPs on SiO_2-WO_3 composites was carried out to modify these WO_3-containing materials with metal nanoparticles. Selective removal of SiO_2 templates with HF afforded pure WO_3 catalysts. Synthetic details for all catalysts in this study can be found in the **Supporting Information**.

Materials characterization. Nitrogen physisorption was carried out at 77 K on a Micromeritics TriStar 3000 surface area and porosity analyzer. Surface areas and pore size distributions were calculated using the BET and BJH methods, respectively. Powder X-ray diffraction (XRD) was performed on a Rigaku MiniFlex II diffractometer using Cu K_α radiation generated with a tube output voltage and current of 30 kV and 15 mA, respectively. The diffractometer was equipped with a water-cooled Scintillator detector that was used at a continuous rate of 0.5° (2θ) per minute. High-resolution transmission electron micrographs were recorded with a JEOL JEM 2100F microscope operating at 200 kV. Samples were dispersed in methylchloride and transferred to carbon coated copper grids prior to analysis. Energy dispersive X-ray spectroscopy (EDS) elemental analysis of samples was done with an Oxford INCA system attached to the same microscope. X-ray photoelectron spectroscopy (XPS) was carried out using a Physical Electronics PHI 5700 spectrometer with non-monochromatic Mg Kα radiation (300 W, 15 kV, 1253.6 eV) for the analysis of photoelectronic signals of C 1s, O 1s, Si 2p, Au 4f and W 4f with a multi-channel detector. Additional experimental details regarding the XPS analyses can be found in reference 36. Elemental analysis by inductively-coupled plasma optical emission spectroscopy (ICP-OES) was completed on a PerkinElmer Optima 7000DV ICP optical emission spectrometer with a CCD array detector, a PerkinElmer S10 autosampler, and WinLab32 software. Details of the ICP-OES sample preparation can be found in the **Supporting Information**. Concentrated ammonium hydroxide (29 wt%) was obtained from Fisher Scientific. Chloroauric acid trihydrate ($HAuCl_4 \bullet 3H_2O$, ACS reagent, 99.99%) was purchased from Alfa Aesar. All other chemicals were obtained from Sigma-Aldrich. All chemicals were used as received.

Ammonia temperature-programmed desorption (NH_3-TPD). Experiments were conducted on a Micromeritics Chemisorb 2720 chemisorption analyzer equipped with a thermal conductivity detector (TCD) and a ChemiSoft TPx system for temperature control and data analysis. Samples were analyzed as powders positioned between two beds of quartz wool in a U-shaped quartz tube. Catalysts (0.05 g) were pretreated under N_2 flow at 460 °C for 2 h and then cooled to 100 °C under the same flow. Pretreated samples were then exposed to anhydrous NH_3 at 100 °C for 1 h followed by a flow of N_2 at the same temperature for 1 h to desorb weakly physisorbed NH_3. The temperature was then increased from 100 °C to 600 °C at 10 °C min^{-1} while monitoring desorbed NH_3. All gas flow rates were 30 cm^{-3} min^{-1}.

Hydrogen temperature-programmed reduction (H_2-TPR). Tests were carried out on powdered samples using the same analyzer as in NH_3-TPD experiments (see above). Catalysts (0.05 g) were pretreated under N_2 flow at 130 °C for 2 h and then cooled to 50 °C under the same flow. Pretreated samples were then reduced with 10% H_2/Ar at a heating ramp of 10 °C min^{-1} to 1000 °C while monitoring H_2 consumption. Water vapor was collected downstream of the quartz tube reactor using a NaCl/ice bath upstream from the TCD. All gas flow rates were 30 cm^3 min^{-1}.

Methanol aerobic transformation catalysis. Catalytic methanol transformation tests were carried out under aerobic conditions at atmospheric pressure in a fixed bed quartz tube reactor (i.d. 12 mm, length 400 mm). Catalyst samples (0.1 g, 0.25 – 0.60 mm particle size) were mixed with 2 g of silicon carbide (0.75 mm particle size) to maintain a constant volume within the catalyst bed. The feed gas consisted of a mixture of methanol/oxygen/nitrogen in a 6:13:81 molar ratio. The flow rate was 100 cm^3 min^{-1}. Experiments were carried out from 108 – 375 °C to obtain the greatest conversion of methanol. Reactants and reaction products were characterized online with gas chromatography using Rt®-U-BOND (fused silica PLOT, length 30 m, i.d. 0.53 mm) and HP-Molesieve (length 30 m, i.d. 0.53 mm) columns.

Results and Discussion

Catalyst synthesis and characterization. The preparation of porous Au-loaded and non-loaded WO_3 catalysts were carried out as described in our recently published work,[37] with minor adjustments (**Scheme 1**).

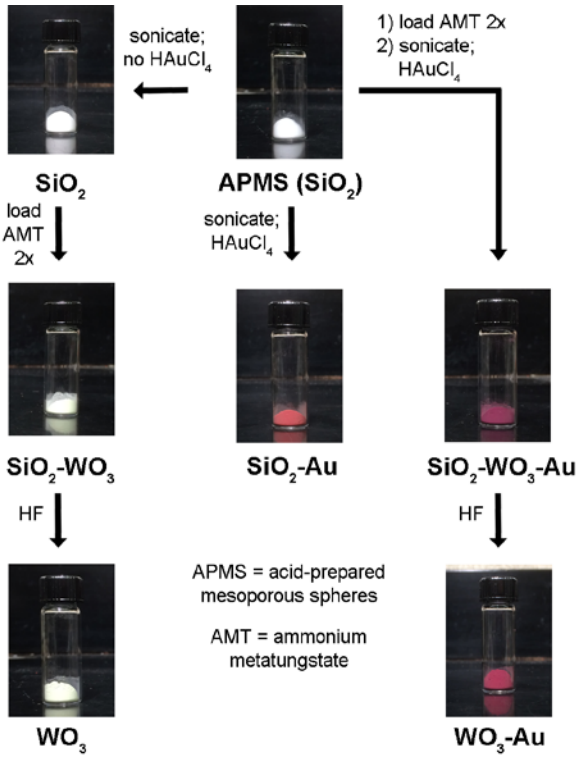

Scheme 1. Synthesis scheme for the various porous materials studied in this work.

Starting with acid-prepared mesoporous spheres (APMS) of silica, well-dispersed gold nanoparticles (Au NPs) were sonochemically deposited within the porous SiO_2 particles to yield SiO_2-Au. Tungsten oxide (WO_3) and Au NPs were added to APMS in a two-step process: first, APMS was twice impregnated

with ammonium metatungstate (AMT) via incipient wetness and calcined to crystallize WO_3, and then Au NPs were sonochemically deposited to form SiO_2-WO_3-Au catalysts. For catalysts not containing Au NPs (i.e. SiO_2-WO_3 and WO_3), APMS was subjected to a sonochemical treatment in the absence of $HAuCl_4 \bullet 3H_2O$ and then calcined at 500 °C before continuing with WO_3 incorporation. In some cases, catalysts with lower loadings of Au NPs were prepared and characterized (designated SiO_2-Au^L and SiO_2-WO_3-Au^L). Etching of SiO_2-WO_3 and SiO_2-WO_3-Au composites with HF led to pure WO_3 and WO_3-Au catalysts, respectively, as confirmed by ICP-OES.

Powder X-ray diffraction (**Figure 1**) was used to study the crystallinity of the prepared catalysts after calcination. It was apparent that all catalysts containing WO_3 were nanocrystalline in nature, which was expected due to ammonium metatungstate decomposition during calcination to form monoclinic WO_3 (ICDD No. 00-043-1035).

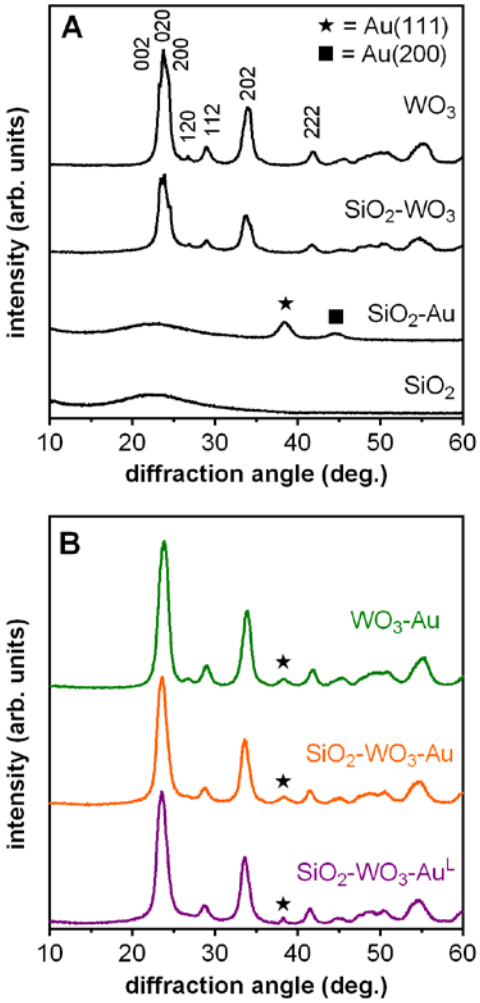

Figure 1. Powder X-ray diffraction patterns of (A) catalysts containing only Au NPs or WO_3 and (B) catalysts loaded with both Au NPs and WO_3. Monoclinic WO_3 (ICDD No. 00-043-1035) phases are indicated in (A).

Scherrer calculations of the broadened diffraction peaks yielded WO_3 crystallite sizes of 6 – 12 nm; combined with the larger crystallite sizes observed by TEM (see below), this was an indication of the polycrystalline nature of the WO_3 aggregates. An additional broad feature at 38° assigned to the Au(111) plane was evidence of crystalline Au nanoparticles loaded within the different catalysts. It was clear that the sonochemical deposition of Au NPs onto SiO_2-WO_3 did not have a significant effect on the crystallinity of WO_3. Gold nanoparticle sizes of 5 – 12 nm were determined by XRD depending on the substrate on which the Au NPs were deposited. The larger Au NPs found in SiO_2-WO_3-Au^L as compared to SiO_2-WO_3-Au can be explained by the differences in the synthesis pH of these catalysts. A consistent NH_3 : Au mole ratio of 250 : 1 was used during the preparation of SiO_2-WO_3-Au and SiO_2-WO_3-Au^L. Therefore, lower concentrations of both NH_3 and $HAuCl_4 \bullet 3H_2O$ were used during the synthesis of SiO_2-WO_3-Au^L, which decreased the pH relative to SiO_2-WO_3-Au. Although the nominal Au wt% loading was lower for SiO_2-WO_3-Au^L, this lower synthesis pH (pH = 8.97) yielded larger Au NPs of (12 nm) compared to SiO_2-WO_3-Au, which was prepared at pH = 9.89. In contrast, the higher pH during the preparation of SiO_2-WO_3-Au favored deposition of 7 nm Au NPs even at a higher wt% loading.[38] Future work will address these size differences by focusing on maintaining similar pH conditions with changing Au loadings.

Transmission electron microscopy (TEM) and scanning transmission electron microscopy (STEM) were used to provide further details of the crystalline nature of the catalysts loaded with WO_3 and Au (**Figure 2**). Highly dispersed Au NPs were observed throughout the catalysts after calcination, and the approximate sizes of the Au NPs were in agreement with the XRD data. It was clear from the micrograph of SiO_2-Au^L that 5 – 6 nm Au were deposited evenly throughout the larger spherical SiO_2 particles. These Au NP sizes were also found in SiO_2-Au (not shown). TEM measurements showed that SiO_2-WO_3-Au possessed Au NPs with average diameters of 5 nm, which were similar to SiO_2-Au. Regions of smaller Au NP clusters (1 – 2 nm) could also be observed, as well as slightly larger Au NPs that had sizes in agreement with the Scherrer calculations from the XRD data of SiO_2-WO_3-Au. Less favorable interactions between Au NPs and WO_3 crystallites with low surface isoelectric points (IEP) are thought to cause Au NP growth during the calcination treatment.[37] The overall spherical morphology of the SiO_2-WO_3-Au microparticles was also confirmed by TEM. Large crystallites of WO_3 were present on the outer surface of the microparticles, which made it clear that some WO_3 was not incorporated inside the pores of the porous silica (Supporting Information, **Figure S1**). However, energy dispersive X-ray spectroscopy (EDS) analysis of the spherical SiO_2-WO_3-Au catalyst (**Figure S2**) revealed that Au NPs were present in both SiO_2 and WO_3 matrices within the composite microparticles, which was in accordance with our previous studies of similar materials.[37] The nanocrystalline nature of the catalysts was studied further with high-resolution TEM; as an example, HR-TEM of WO_3-Au is shown in **Figure 2**. The *d*-values between

lattice fringes within WO_3 nanoparticles were 0.30 nm, which corresponded to the monoclinic WO_3(112) plane. Likewise, the 0.23 nm spacing of Au(111) planes were apparent in highly crystalline Au NPs that were slightly larger than 5 nm. These *d*-spacing measurements matched the values obtained from the peaks for WO_3 and Au observed in the XRD data.

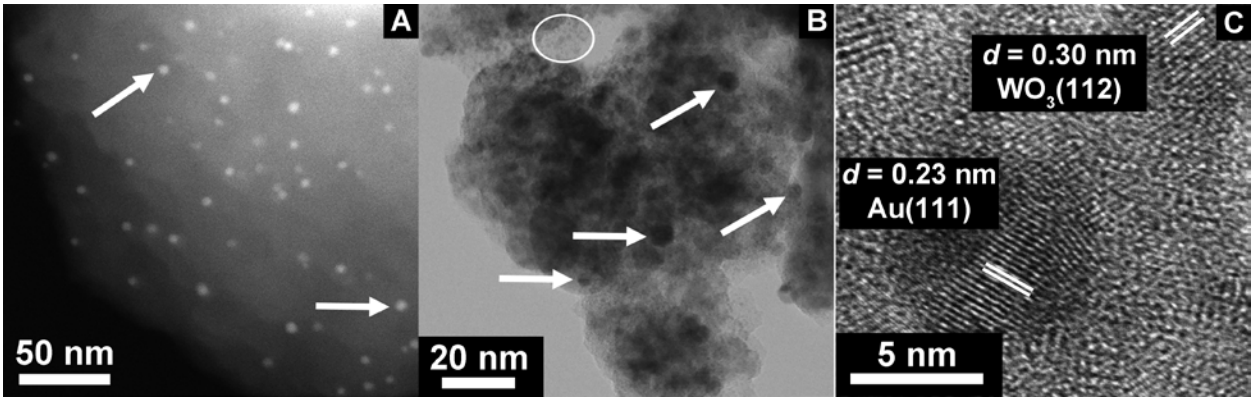

Figure 2. (A) Dark-field STEM micrograph of SiO_2-Au^L, (B) bright-field STEM micrograph of SiO_2-WO_3-Au, and (C) HR-TEM of WO_3-Au. Arrows denote individual Au nanoparticles. The white circle highlights a region containing smaller (1-2 nm) Au nanoparticle clusters in SiO_2-WO_3-Au.

The 4f Au XPS spectra for SiO_2-Au and WO_3-Au are shown in **Figure 3**. Both catalysts showed the Au $4f_{5/2}$ and Au $4f_{7/2}$ doublet for Au^0 species. Although formal spectral features of Au^+ and Au^{3+} were not observed, the energy of the Au $4f_{7/2}$ peak for SiO_2-Au was 83.2 eV, while the corresponding peak for WO_3-Au was shifted to higher energies (83.8 eV). This same trend was observed for the Au $4f_{5/2}$ peak, which appeared at 86.7 eV and 87.5 eV for SiO_2-Au and WO_3-Au, respectively. This energy shift of approximately 0.6 – 0.8 eV was consistent with the presence of some Au^+ on WO_3.[39,40] Cationic Au indicated a stronger electronic interaction between Au/WO_3 than Au/SiO_2. The Si/W, W/Au, and Au/Si atomic ratios determined by XPS for various catalysts are summarized in **Table S1**.

Inductively-coupled plasma optical emission spectroscopy (ICP-OES) was used to study the catalyst composition at various stages of preparation (**Table 1**). The incorporation of crystalline WO_3 was supported by the expected increase in W (wt%), and etching of the SiO_2 template was shown by the significantly lower Si/W ratio for WO_3 compared to SiO_2-WO_3. Using this sonochemical method, fairly high loadings of Au (> 3.5 wt%) were obtained in the Au NP modified catalysts. The slight increase in the Si/W ratio from SiO_2-WO_3 to SiO_2-WO_3-Au meant that WO_3 dissolved to a greater extent than SiO_2 during the sonochemical deposition of Au NPs under basic conditions. In the end, it was clear that a large amount of WO_3 was preserved in the Au-loaded catalysts after deposition of Au NPs, even in solutions containing NH_3. Similar to SiO_2-WO_3 described above, the HF treatment of SiO_2-WO_3-Au was successful in removing the SiO_2 portion of this material to afford WO_3-Au (Si/W = 0.02).

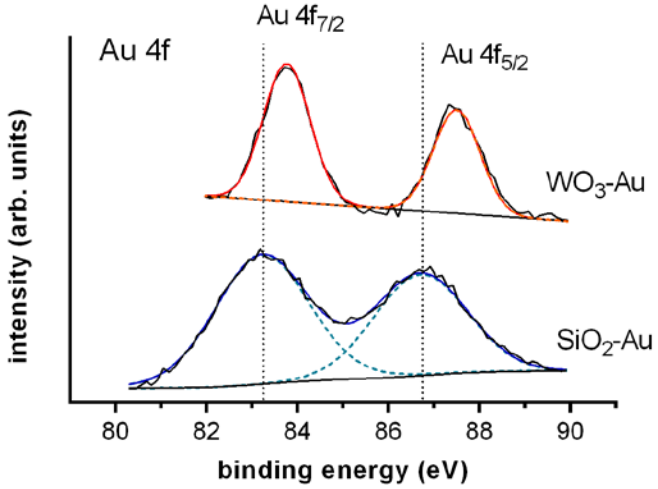

Figure 3. Au 4f XPS spectra of WO_3-Au and SiO_2-Au catalysts. The dotted lines are shown to highlight the shift in the Au $4f_{7/2}$ and Au $4f_{5/2}$ bands when comparing the two catalysts.

Table 1. Summary of elemental analysis, gold nanoparticle size, and N_2 physisorption data of the catalysts studied in this work.

Sample	ICP-OES				XRD/TEM	N_2 physisorption		
	W (wt%)	Au (wt%)	Si/W (mole ratio)	W/Au (mole ratio)	Au size (nm)	SA_{BET} ($m^2\ g^{-1}$)	V_{pore} ($cm^3\ g^{-1}$)	d_{pore} (Å)
SiO_2						494	0.66	58
SiO_2-WO_3	56.7		1.54			81	0.09	36
WO_3	78.4		0.02			62	0.15	64
SiO_2-Au		3.74			5 [a]	478	0.69	57
SiO_2-Au^L		0.55			5 – 6 [a,b]	489	0.80	72
SiO_2-WO_3-Au	54.4	3.53	1.63	16.5	5 – 7 [a,b]	87	0.14	43
SiO_2-WO_3-Au^L	52.0	0.62	2.03	89.3	12 [a]	122	0.17	43
WO_3-Au	74.5	4.74	0.02	16.8	8 [a]	73	0.21	28

[a] Measured by XRD. [b] Measured by TEM. [L] Lower Au wt% loading.

The porosity of the studied catalysts was probed by N_2 physisorption, and the results are summarized in **Table 1**. Associated physisorption isotherms (**Figure S3**) and pore size distributions (**Figure S4**) can be found in the **Supporting Information**. The mesoporous SiO_2 particles contained large pores, which made them a suitable template for WO_3 incorporation. As expected, filling of the pores with high loadings of crystalline WO_3 decreased the porosity of this material. Removal of the SiO_2 template from SiO_2-WO_3 led to pure porous WO_3 catalysts, which had larger pores than the composite. It is relevant to note the very broad external pore size distributions for these catalysts. Irregular voids between the aggregated WO_3 crystallites forming the pores in porous WO_3 caused pore distributions to be non-uniform in all cases. The reported pore diameters are the observed maxima in these distributions, but it was apparent that the pore sizes varied widely over 100 – 200 Å and showed multiple features depending on the material. Comparing SiO_2-WO_3 and SiO_2-WO_3-Au, a significant broadening of the pore size distribution was observed after Au loading. A combination of SiO_2 and WO_3 dissolution during this process led to the

formation of larger irregular pores, whereas Au deposition had a lesser effect on the porosity of SiO_2-WO_3-Au.

Catalyst acid site characterization. Ammonia temperature-programmed desorption (NH_3-TPD) is a commonly used method to analyze the surface acidity of various catalysts.[5,41-43] **Figure 4** shows the NH_3-TPD traces of several representative catalysts containing WO_3. Pure mesoporous SiO_2 (not shown) showed a weak feature at 120 °C that corresponded to the desorption of weakly bound NH_3 over weakly acidic SiO_2.[5] The broad feature at 200 °C in SiO_2- and WO_3-containing composites (solid lines) signified the introduction of different, slightly stronger acid sites on these catalysts compared to SiO_2. These new features may correspond to substitution of W in the amorphous SiO_2 framework. Higher temperature (> 500 °C) features indicated desorption of NH_3 from strong acid sites on these composite SiO_2-WO_3 catalysts. Desorption of H_2O from surface dehydroxylation at temperatures above the calcination temperature (500 °C) may also explain this observation. After removal of the SiO_2 template, it was clear that pure WO_3 catalysts possessed moderate acidity. Two resolved features at 170 °C and 260 °C suggested that there may be both weak and medium strength acid sites on these catalysts,[41] which were not affected by the presence of Au NPs. Strong acidity was not observed over pure WO_3 catalysts as shown by the absence of peaks at temperatures > 500 °C. From this data, it was expected that these acidic WO_3 catalysts would be beneficial in the selective dehydration of methanol to dimethyl ether.[14,15,41] Importantly, Au NPs did not affect the acidity of the WO_3-containing catalysts, as determined by NH_3-TPD. During methanol transformation catalysis, however, Au NPs influenced the activity and selectivity of the WO_3 catalysts, which is discussed below.

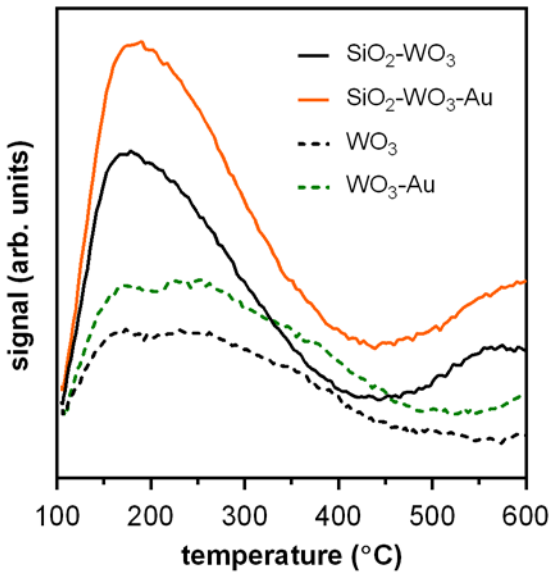

Figure 4. NH_3-TPD traces for Au-modified and non-modified catalysts in the composite (SiO_2-WO_3, solid lines) and pure (WO_3, dashed lines) forms.

Catalyst reducibility characterization by H_2-TPR. The reducibility of the catalysts was monitored by H_2 temperature-programmed reduction (H_2-TPR). The oxide reducibility can be informative in regards to describing the relative reactivity of the SiO_2-WO_3 and WO_3 catalysts. In general, peaks appearing at lower temperatures in a TPR profile indicate more facile reduction events occurring within the metal oxide. The TPR profiles of various Au-modified and non-modified catalysts are shown in **Figure 5**. A control sample, SiO_2-Au, did not show any reduction events. Silica is a non-reducible oxide in this temperature range, and Au was in its fully reduced metallic state as Au^0 NPs, in agreement with the XRD, XPS, and TEM data.

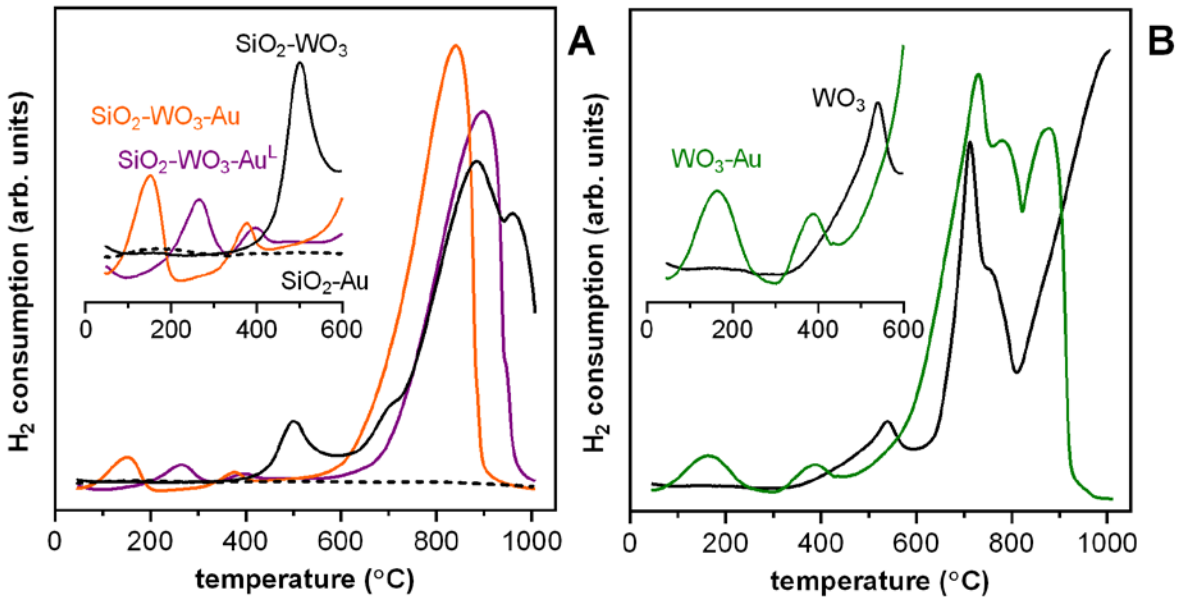

Figure 5. H_2-TPR traces of (A) SiO_2-WO_3 and (B) WO_3 catalysts both with and without loaded Au NPs. Insets are expansions of regions from 0 – 600 °C.

Materials containing WO_3, however, displayed multiple reduction events up to 1000 °C. The position and resolution of the peaks for the various catalysts depended on the stability of the reduced WO_x species within the materials. In the non-modified SiO_2-WO_3 composite and pure WO_3, three major regions of reduction were observed. The peak near 500 – 550 °C can be attributed to the reduction of surface oxygens on WO_3 to form substoichiometric $WO_{2.9}$ surface species. This was followed by a bulk reduction step from $WO_{2.9}$ to WO_2 from 700 – 900 °C, and then a final reduction of WO_2 to W^0 near 1000 °C.[4,44]

Clearly, WO_3 catalysts not loaded with Au NPs displayed different TPR profiles than those loaded with Au NPs. Initial WO_3 surface reduction ($WO_3 \rightarrow WO_{2.9}$) was more facile for SiO_2-WO_3-Au and SiO_2-WO_3-Au^L than SiO_2-WO_3 (**Figure 5A**, inset). It appeared that this WO_3 reduction event shifted to lower temperatures and resolved into two separate features in the temperature range of 100 – 250 °C in the

presence of Au NPs. This result suggested that there were significant Au—O—W interactions on the surface of these catalysts, which led to weakened surface W—O bonds.[33,45] The formation of two separate reduction events indicated the presence of two stable WO_x species during reduction in this temperature range. Increased Au NP loading caused the features to shift to lower temperatures, which meant increased oxygen reducibility.[33] However, the larger Au NPs of SiO_2-WO_3-Au^L may also affect the WO_3 reducibility differently than smaller Au NPs. As shown in the inset of **Figure 5B**, similar behavior was seen in WO_3-Au, which has increased surface oxygen reducibility compared to WO_3. Dissociation of H_2 over Au NPs or reduced WO_{3-x}[30] and other electronic effects increased the reducibility of the surface oxygen of WO_3, which led to oxygen vacancies at the catalyst surface.[27] This result was expected to have implications on the reactivity of the Au-loaded WO_3 catalysts in methanol transformation reactions. Specifically, facile removal of lattice oxygen from the WO_3 surface will introduce oxidation reactivity to these Au-loaded catalysts as will be discussed below.

The bulk reduction events of WO_3 were also impacted by Au NPs loaded on the surface of the catalysts. Interestingly, this observation is in contrast to reports of Au/CeO_2, in which Au NPs only affected the reduction surface ceria species, but not the bulk.[34,35] In the presence of Au NPs, the WO_3 species were generally more reducible than without Au NPs, as shown by the shifting of reduction events to lower temperatures. Complete reduction to W^0 was shown at temperatures below 1000 °C for Au-loaded catalysts, but SiO_2-WO_3 and WO_3 were not completely reduced up to 1000 °C. Also, there were significant changes in the TPR profile shapes when comparing Au-loaded and non-loaded catalysts. SiO_2-WO_3-Au and SiO_2-WO_3-Au^L showed a single broad reduction event in the 800 – 900 °C region, while pure WO_3 and WO_3-Au catalysts showed resolved features and at slightly lower temperatures (700 – 800 °C). The increased peak resolution in the bulk region of pure WO_3 catalysts may indicate increased stabilization of tungsten oxides with intermediate oxidation states. Overall, it was apparent that Au NPs loaded on the surface of these catalysts led to more easily reduced surface and bulk WO_3 species.

Methanol transformation activity studies. Catalytic gas-phase methanol transformation reactions were conducted under aerobic conditions in the presence of various Au-loaded and non-loaded catalysts. Pure SiO_2 does not possess significant acid or redox sites, and thus the activity of this material was negligible, which agreed with the NH_3-TPD and H_2-TPR data. However, SiO_2-Au was very reactive, showing increasing activity as the loading of Au increased. Considering equal contact times between all catalysts, the Au-loaded catalysts showed greater conversions at lower temperatures than the non-loaded catalysts (**Figure S5**). These results showed the significant role that Au NPs played in converting MeOH at lower temperatures. The SiO_2-WO_3-Au^L catalyst was an exception to this trend, however. The lower activity of this catalyst is most likely attributed to the lower Au loading, the larger Au NP sizes (~12 nm), and the

greater W/Au mole ratio associated with this material. Therefore, it seemed beneficial to use catalysts that possess smaller dispersed Au NPs for this catalytic reaction.

To compare the activity of Au-loaded and non-loaded catalysts, the rates of MeOH conversion were determined for several catalysts at similar temperatures (234 – 247 °C) and contact times (**Table 2**). To make more complete comparisons between the WO_3 and WO_3-Au catalysts, additional MeOH conversion rates were determined at lower reaction temperatures (**Table S2**). The catalytic rates and the selectivity distributions (*vide infra*) were compared using slightly different temperatures and conversions because of the exothermic nature of this reaction and the high reactivity of the studied catalysts. For these reasons, large temperature gradients at the catalyst were observed.

Table 2. Rates of methanol (MeOH) conversion for Au-loaded and non-loaded catalysts.

Catalyst	Temp. (°C)	X_{MeOH} (%)	rate MeOH conversion [a] $mmol_{MeOH}\ h^{-1}\ g_{cat}^{-1}$	$mmol_{MeOH}\ h^{-1}\ g_W^{-1}$	$mmol_{MeOH}\ h^{-1}\ g_{Au}^{-1}$	$mmol_{MeOH}\ h^{-1}\ (m_{cat})^{-2}$ [b]
SiO_2-Au	241	47.0	138	---	3696	0.289
SiO_2-WO_3-Au	234	17.3	25.8	47.5	731	0.297
SiO_2-WO_3-Au^L	247	3.5	5.22	10.0	843	0.043
SiO_2-WO_3	239	9.2	13.7	24.2	---	0.170
WO_3-Au	246	66.9	99.9	134	2107	1.368
WO_3	239	12.6	18.8	24.0	---	0.303

[a] Contact time (W/F) = 6.7 g_{cat} h $(mol_{MeOH})^{-1}$ for all catalysts except for sample SiO_2-Au (W/F = 3.4 g_{cat} h $(mol_{MeOH})^{-1}$)
[b] Calculated using the surface area of catalyst

The SiO_2-Au sample was clearly the most active catalyst, which indicated that Au NPs are responsible for increased reaction rates at lower temperatures. Comparisons of SiO_2-Au and SiO_2-WO_3 reaction rates exhibited the greater activity of Au NPs relative to WO_3 nanocrystals. Also, the greater surface area and accessible porosity of SiO_2-Au better facilitated MeOH conversion compared to SiO_2-WO_3 catalysts. When WO_3 and Au NPs were added to the SiO_2 support (SiO_2-WO_3-Au), the rate per g Au and per m^2_{cat} decreased, illustrating that WO_3 had a negative effect on Au NP activity. This result may be related to the observed XPS shifts in Au 4f band energies for SiO_2-Au and WO_3-Au shown in **Figure 3**, indicating that a more fully reduced Au species is favorable for the MeOH reaction. On the other hand, a significant increase in the rate of conversion per gram of W showed that Au NPs increased the activity of WO_3 species, especially at higher loadings. These more active Au-modified WO_3 species agreed with the more easily reduced WO_3 species observed on SiO_2-WO_3-Au via H_2-TPR (**Figure 5**).

Among SiO_2-WO_3 composite catalysts, the rate of MeOH conversion per gram of total catalyst (g_{cat}^{-1}), per gram of tungsten (g_W^{-1}), and per unit surface area (m^{-2}) was the greatest for SiO_2-WO_3-Au. For the pure WO_3 catalysts, MeOH conversion rates confirmed that WO_3-Au was more active than WO_3, which

agreed with the results for the SiO_2-WO_3 composites. Overall, the features of WO_3-Au made it the most active catalyst containing WO_3. Au NPs clearly increased the activity of all WO_3-containing catalysts.

We sought to further explore the interaction between WO_3 and Au by testing a physical mixture of SiO_2-Au and SiO_2-WO_3. The results of this experiment showed that the activity of the physical mixture mirrored that of SiO_2-Au alone (**Figure S6**). This supported the hypothesis that the negative effects of the WO_3 species on Au NPs originate from the interaction between the two when both are in intimate contact through synthesis.

Methanol dehydration to DME over catalysts without Au NPs. Analysis of the MeOH transformation product selectivity was carried out for the various catalysts. **Figure 6** shows the product distributions for the SiO_2-WO_3 and WO_3 catalysts at both low and high methanol conversions. Very high selectivity (> 60%) to dimethyl ether (DME) was observed over both types of catalysts at all studied conversions. Minor redox products such as formaldehyde (FM), methyl formate (MF), and dimethoxymethane (DMM) were observed. Also, non-selective carbon oxides (CO + CO_2) formation was low (< 18% selectivity) up to 300 – 350 °C. The dehydration reactivity of these catalysts confirmed the moderate acidity of the crystalline WO_3 species, which was supported by the NH_3-TPD data. As with non-crystalline WO_3 and tungsten Keggin heteropoly acid (HPA) catalysts found throughout the literature,[1-4,6,12] these crystalline SiO_2-WO_3 and WO_3 catalysts were very selective to DME, with no significant oxidation reactivity.

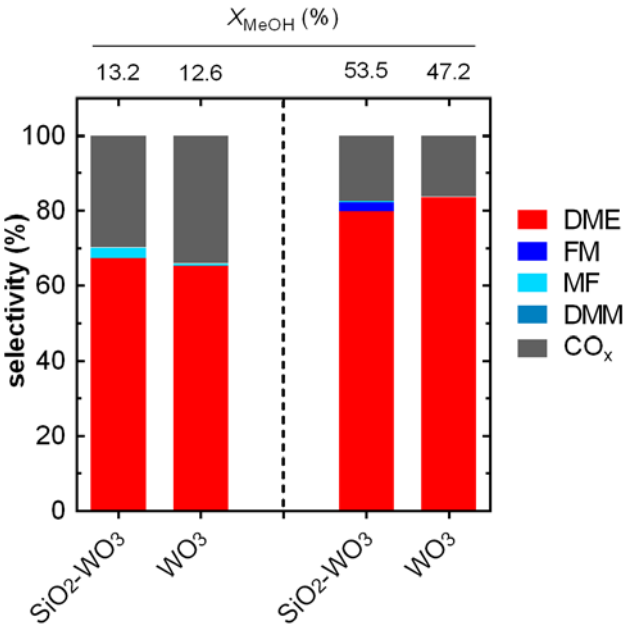

Figure 6. Percent selectivity for the methanol transformation reaction over SiO_2-WO_3 and WO_3 catalysts at (left) low methanol conversions and (right) high methanol conversions. Percent conversions (X_{MeOH}) for each catalyst are shown at top of graphs. See text for abbreviation definitions.

Methanol aerobic transformation over Au-loaded catalysts. The oxidative MeOH transformation on Au-modified catalysts showed significant differences compared to their non-modified counterparts. It was clear that once Au NPs were loaded in the catalysts, MeOH dehydration selectivity decreased at the expense of increased oxidation selectivity. It is unlikely that the Au NPs significantly altered the WO_3 acid sites, as shown by NH_3-TPD experiments (**Figure 4**). However, the Au NPs increased the oxidative reactivity of the modified WO_3 catalysts through increasing the reducibility of WO_3 species and the formation of oxygen vacancies (**Figure 5**). Methanol oxidation reactions over Au-modified WO_3 were more favored than the acid-catalyzed dehydration of MeOH. This led to decreased DME production over Au-loaded catalysts. **Figure 7A** shows the product distributions of various Au-loaded catalysts at low MeOH conversions (7 – 13%). Gold nanoparticles on porous SiO_2 (SiO_2-Au) led to mainly MF production, which is in accordance with the literature on Au catalysts.[46,47] Moreover, dimethyl ether selectivity was not observed in this case.

The product distribution of the SiO_2-WO_3-Au^L catalyst was different than that of SiO_2-WO_3, but the major reaction product was still DME (73.9%) at low methanol conversion. This indicated that the amount of Au in this sample was insufficient to be reactive and have a major impact on the WO_3 acid sites. Indeed, simply altering the loading of Au NPs on these catalysts modulated the reactivity of these catalysts. The Au modified composite catalyst (SiO_2-WO_3-Au) showed a greater variety of oxidation products compared to SiO_2-Au. In addition to MF, FM was observed from the primary oxidation of MeOH, and dimethoxymethane (DMM) was produced from the secondary HCHO-CH_3OH acetalization reaction over WO_3 acid sites. Deep oxidation to CO_x was also more facile with Au NPs coupled to WO_3 as more labile surface oxygen atoms from the WO_3 support reacted with MeOH. In this way, the WO_3-Au showed higher CO_x formation, with a distribution of FM, MF and DMM similar to that observed for sample SiO_2-WO_3-Au suggesting that, in both cases, Au NPs were interacting with WO_3 crystallites.

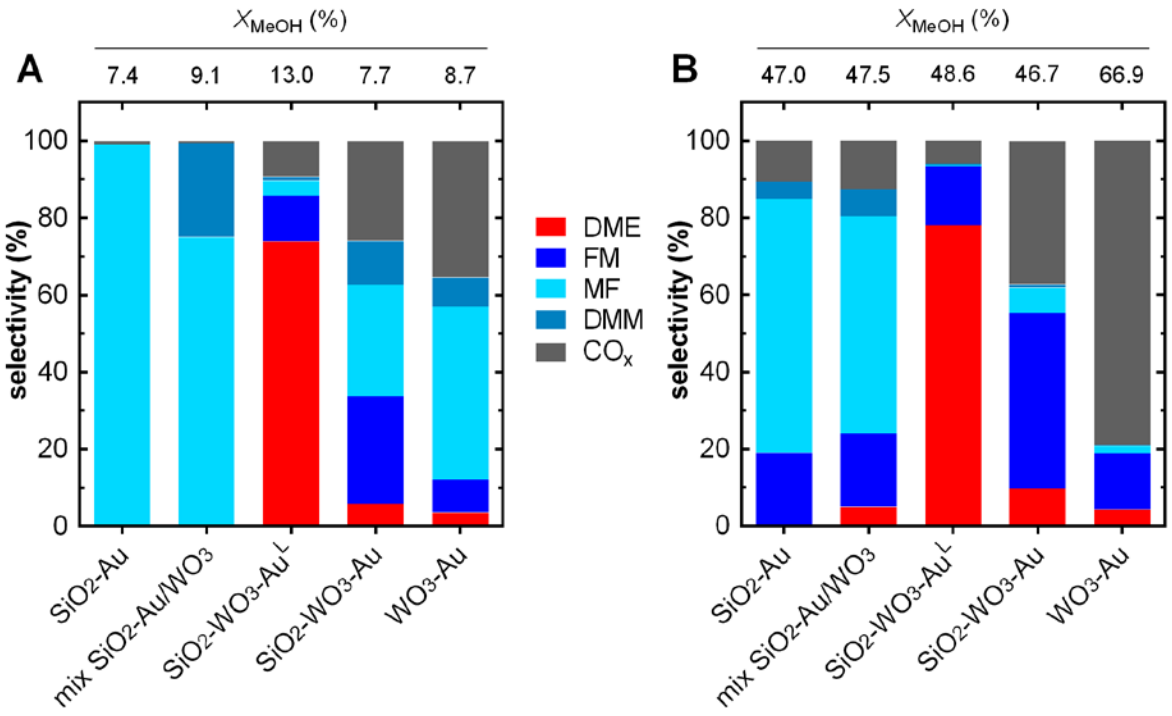

Figure 7. Percent selectivity for the methanol transformation reaction over Au-loaded catalysts at (A) low methanol conversions and (B) high methanol conversions. Percent conversions (X_{MeOH}) for each catalyst are shown at top of each graph. See text for abbreviation definitions.

The SiO_2-Au/SiO_2-WO_3 physical mixture strongly favored MF production and minor DMM formation, which was different from the reactivity observed over SiO_2-WO_3-Au. The DMM selectivity originated from the secondary oxidation product of FM in the presence of WO_3 acid sites. This indicated that the SiO_2-Au reactivity was more accessible and facile than the SiO_2-WO_3 reaction pathway, especially because no DME was observed. Therefore, WO_3 crystallites significantly affected the reactivity of Au NPs when the two species were in intimate contact through synthesis, which agreed with the MeOH conversion results of the physical mixture. Similar product distributions between SiO_2-WO_3-Au and WO_3-Au meant that at low conversions, these two catalysts behaved nearly the same. This oxidation activity was attributed to Au NPs, which had two major effects: the Au NPs (1) activated O_2 in the feed gas[46] and (2) induced more reactive WO_3 surface redox sites,[48] which were confirmed by H_2-TPR. Secondary HCHO-CH_3OH acetalization reactions led to intermediates that can either convert to DMM on acid sites or dehydrogenate to form MF over redox sites on the support.[49,50] This was evidence that the composition of the catalyst support played a major role in the oxidation reactions initiated by the Au NPs. Slightly higher selectivity to CO_x over WO_3-Au compared to SiO_2-WO_3-Au was due to the higher oxidation activity of this catalyst.

At higher MeOH conversions, further changes in the reaction selectivity were observed (**Figure 7B**). Two general differences in selectivity occurred at the higher reaction temperatures used to obtain higher MeOH conversions. First, the production of CO_x increased for most of the catalysts, which was favored at high temperatures under aerobic reaction conditions. Second, DMM was not significantly produced (only a small quantity was detected in the physical mixture catalyst). At higher temperatures, the acidic surface hydroxyl groups on SiO_2-WO_3 and WO_3 became less stable, which led to increasing non-selective oxidation reactions to CO_x in the presence of abundant Au NPs. In addition, primary oxidation of MeOH to FM may be quickly followed by desorption of FM from the catalyst surface or further oxidation to CO_x, whereas further coupling with MeOH to form DMM is less likely at higher MeOH conversions. The exception to this trend was SiO_2-WO_3-Au^L, which showed 78.1% DME selectivity at 48.6% MeOH conversion. This suggested that WO_3 acid sites dominated the MeOH catalysis at lower loadings of Au NPs, as was the case at low MeOH conversions.

In terms of selective oxidation products, FM was favored over the WO_3-containing catalysts, with only small amounts of MF formed. Stabilization of FM species on WO_3 Brønsted acid sites[51] may have prevented further oxidative coupling with MeOH to form MF. Subsequent desorption of FM or further oxidation to CO_x seemed to be favored under these high temperatures and aerobic reaction conditions. Selectivity comparisons between SiO_2-WO_3-Au and WO_3-Au suggested that the pure WO_3 support may have had stronger interactions with surface-bound FM than SiO_2-WO_3 and more abundant active O* from the WO_3 lattice. Thus, the stabilized FM molecules were converted primarily to total oxidation products (CO_x) over the WO_3-Au catalyst. Interestingly, SiO_2-Au remained highly selective to MF, highlighting the unique reactivity of Au NPs on inert supports. Overall, FM was only observed in the presence of Au NPs and WO_3, which can be correlated to the presence of more reducible WO_3 species as shown by H_2-TPR.

Scheme 2 displays the possible reaction pathways observed in this study. It was clear that the catalyst composition could be tuned to alter the activity and selectivity towards MeOH transformations. Over acid sites, MeOH was dehydrated to DME over all catalysts that contained WO_3 and low loadings of Au NPs. Increasing the Au wt% loading caused MeOH oxidation to occur more favorably at the expense of dehydration reactivity. At low conversions and in the presence of acidic WO_3, DMM was favored, but at high conversions, FM was the major oxidation product. A combination of strongly adsorbed FM, less stable acid sites, and high MeOH conversions effectively diminished the oxidative coupling (MF) and non-oxidative condensation (DMM) pathways. Therefore, primary oxidation to FM and total oxidation to CO_x were observed in the presence of excess O* (both labile lattice O and activated O from the feed gas) and high temperatures. Methanol oxidation can be seen as a three step process that involves (1) the dissociation of MeOH to methoxy on the metal oxide surface, (2) the activation of the methoxy species by

lattice oxygen, which causes oxygen vacancy formation and subsequent reduction of the oxide, and (3) the re-oxidation of the catalyst by O_2 in the feed.[48,52] In theory, the combination of increased lattice oxygen reactivity and the acidic nature of the catalyst surface could be further optimized for these materials, which makes them very interesting as selective oxidation catalysts in future studies.

Scheme 2. Possible catalytic reaction pathways for the aerobic methanol transformation reaction described in this paper. Adapted from reference [49].

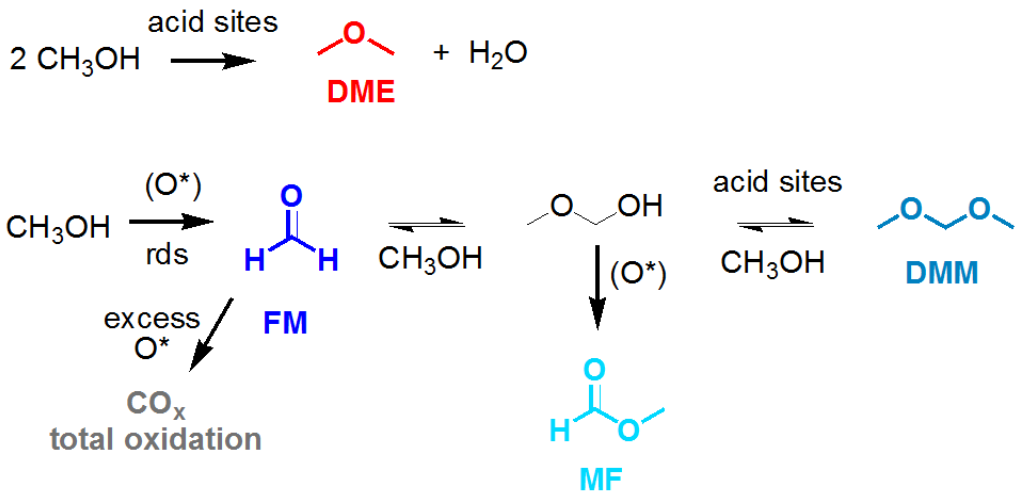

Conclusions

Porous nanocrystalline WO_3-containing catalysts were prepared by a hard templating process and further modified with Au nanoparticles through a sonochemical approach. The acidic WO_3 species in catalysts without Au nanoparticles allowed for highly selective methanol dehydration reactivity while minimizing oxidation pathways at higher temperatures and conversions. Catalysts with Au nanoparticles at higher Au wt% loadings displayed greater catalytic activity in the aerobic transformation of methanol. No differences in WO_3 structure and acidity (as determined by NH_3-TPD) were observed when comparing Au-loaded and non-loaded catalysts. Changes in catalyst redox properties were confirmed by TPR and showed that Au nanoparticles directly affected the reducibility of crystalline WO_3. Specifically, the WO_3 species are more easily reduced with increasing Au loadings. However, WO_3 species decreased the reactivity of supported Au NPs possibly through an electron-withdrawing effect to form oxidized surface Au. Oxidation of methanol to formaldehyde, methyl formate, dimethoxymethane, and CO_x over Au-loaded catalysts agreed with the observation of more labile lattice oxygen from easily reduced WO_3. The Au loading and the temperature of reaction had significant effects on the oxidation product distribution.

Associated Content

Supporting Information

The following information is available free of charge on the ACS Publications website at doi:___: catalyst synthesis details, ICP-OES sample preparation procedures, additional transmission electron microscopy (TEM) images, energy dispersive X-ray spectroscopy (EDS) plots, XPS atomic ratios for various samples, N_2 physisorption isotherms and pore size distributions, methanol conversion as a function of reaction temperature for various catalysts, and methanol conversion rates for WO_3 and WO_3-Au catalysts at lower reaction temperatures.

Author Information

Corresponding Author

E-mail for C.C.L.: christopher.landry@uvm.edu

Notes

The authors declare no competing financial interests.

Acknowledgments

The authors would like to thank the University of Vermont and the DGICYT in Spain (CTQ2015-68951-C3-1-R, CTQ2012-37925-C3-3-R, and SEV-2012-0267 Severo Ochoa Projects) for financial support and David M. Parker for assistance with catalyst synthesis.

References

(1) Macht, J.; Iglesia, E. *Phys. Chem. Chem. Phys.* **2008**, *10*, 5331-5343.
(2) Herrera, J. E.; Kwak, J. H.; Hu, J. Z.; Wang, Y.; Peden, C. H. F.; Macht, J.; Iglesia, E. *J. Catal.* **2006**, *239*, 200-211.
(3) Chauvin, J.; Thomas, K.; Clet, G.; Houalla, M. *J. Phys. Chem. C* **2015**, *119*, 12345-12355.
(4) Barton, D. G.; Soled, S. L.; Meitzner, G. D.; Fuentes, G. A.; Iglesia, E. *J. Catal.* **1999**, *181*, 57-72.
(5) Klepel, O.; Böhlmann, W.; Ivanov, E. B.; Riede, V.; Papp, H. *Microporous Mesoporous Mater.* **2004**, *76*, 105-112.
(6) Macht, J.; Baertsch, C. D.; May-Lozano, M.; Soled, S. L.; Wang, Y.; Iglesia, E. *J. Catal.* **2004**, *227*, 479-491.
(7) Baertsch, C. D.; Komala, K. T.; Chua, Y.-H.; Iglesia, E. *J. Catal.* **2002**, *205*, 44-57.
(8) Wachs, I. E.; Kim, T.; Ross, E. I. *Catal. Today* **2006**, *116*, 162-168.
(9) Kim, T.; Burrows, A.; Kiely, C. J.; Wachs, I. E. *J. Catal.* **2007**, *246*, 370-381.
(10) Ross-Medgaarden, E. I.; Knowles, W. V.; Kim, T.; Wong, M. S.; Zhou, W.; Kiely, C. J.; Wachs, I. E. *J. Catal.* **2008**, *256*, 108-125.
(11) Fang, Z.; Li, Z.; Kelley, M. S.; Kay, B. D.; Li, S.; Hennigan, J. M.; Rousseau, R.; Dohnálek, Z.; Dixon, D. A. *J. Phys. Chem. C* **2014**, *118*, 22620-22634.
(12) Alharbi, W.; Kozhevnikova, E. F.; Kozhevnikov, I. V. *ACS Catal.* **2015**, *5*, 7186-7193.

(13) Nakka, L.; Molinari, J. E.; Wachs, I. E. *J. Am. Chem. Soc.* **2009**, *131*, 15544-15554.
(14) Choi, H.; Lee, E.; Jin, M.; Park, Y.-K.; Kim, J. M.; Jeon, J.-K. *J. Nanosci. Nanotechnol.* **2014**, *14*, 8828-8833.
(15) Sun, J.; Yang, G.; Yoneyama, Y.; Tsubaki, N. *ACS Catal.* **2014**, *4*, 3346-3356.
(16) Ladera, R.; Finocchio, E.; Rojas, S.; Busca, G.; Fierro, J. L. G.; Ojeda, M. *Fuel* **2013**, *113*, 1-9.
(17) Semelsberger, T. A.; Ott, K. C.; Borup, R. L.; Greene, H. L. *Appl. Catal., B* **2006**, *65*, 291-300.
(18) Takeishi, K.; Suzuki, H. *Appl. Catal., A* **2004**, *260*, 111-117.
(19) Fu, Y.; Hong, T.; Chen, J.; Auroux, A.; Shen, J. *Thermochim. Acta* **2005**, *434*, 22-26.
(20) Raoof, F.; Taghizadeh, M.; Eliassi, A.; Yaripour, F. *Fuel* **2008**, *87*, 2967-2971.
(21) Skliri, E.; Lykakis, I. N.; Armatas, G. S. *RSC Adv.* **2014**, *4*, 46170-46178.
(22) Kim, D.-W.; Kim, H.; Jung, Y.-S.; Kyu Song, I.; Baeck, S.-H. *J. Phys. Chem. Solids* **2008**, *69*, 1513-1517.
(23) Hammond, C.; Straus, J.; Righettoni, M.; Pratsinis, S. E.; Hermans, I. *ACS Catal.* **2013**, *3*, 321-327.
(24) Bera, R.; Koner, S. *Inorg. Chim. Acta* **2012**, *384*, 233-238.
(25) Kamata, K.; Yonehara, K.; Sumida, Y.; Hirata, K.; Nojima, S.; Mizuno, N. *Angew. Chem. Int. Ed.* **2011**, *50*, 12062-12066.
(26) Yang, X.-L.; Gao, R.; Dai, W.-L.; Fan, K. *J. Phys. Chem. C* **2008**, *112*, 3819-3826.
(27) Zheng, H.; Ou, J. Z.; Strano, M. S.; Kaner, R. B.; Mitchell, A.; Kalantar-zadeh, K. *Adv. Funct. Mater.* **2011**, *21*, 2175-2196.
(28) Cui, X.; Shi, J.; Chen, H.; Zhang, L.; Guo, L.; Gao, J.; Li, J. *J. Phys. Chem. B* **2008**, *112*, 12024-12031.
(29) Huang, Z.-F.; Song, J.; Pan, L.; Zhang, X.; Wang, L.; Zou, J.-J. *Adv. Mater.* **2015**, *27*, 5309-5327.
(30) Song, J. J.; Huang, Z. F.; Pan, L.; Zou, J. J.; Zhang, X. W.; Wang, L. *ACS Catal.* **2015**, *5*, 6594-6599.
(31) Molkenova, A.; Sarip, R.; Sathasivam, S.; Umek, P.; Vallejos, S.; Blackman, C.; Hogarth, G.; Sankar, G. *Sci. Technol. Adv. Mater.* **2014**, *15*, 065004.
(32) Horváth, D.; Toth, L.; Guczi, L. *Catal. Lett.* **2000**, *67*, 117-128.
(33) Fu, Q.; Weber, A.; Flytzani-Stephanopoulos, M. *Catal. Lett.* **2001**, *77*, 87-95.
(34) Fu, Q.; Kudriavtseva, S.; Saltsburg, H.; Flytzani-Stephanopoulos, M. *Chem. Eng. J.* **2003**, *93*, 41-53.
(35) Andreeva, D.; Idakiev, V.; Tabakova, T.; Ilieva, L.; Falaras, P.; Bourlinos, A.; Travlos, A. *Catal. Today* **2002**, *72*, 51-57.
(36) Botella, P.; García-González, E.; Solsona, B.; Rodríguez-Castellón, E.; González-Calbet, J. M.; López Nieto, J. M. *J. Catal.* **2009**, *265*, 43-53.
(37) DePuccio, D. P.; Botella, P.; O'Rourke, B.; Landry, C. C. *ACS Appl. Mater. Interfaces* **2015**, *7*, 1987-1996.
(38) Elliott, E. W.; Haben, P. M.; Hutchison, J. E. *Langmuir* **2015**, *31*, 11886-11894.
(39) Corma, A.; Garcia, H. *Chem. Soc. Rev.* **2008**, *37*, 2096-2126.
(40) Si, R.; Flytzani-Stephanopoulos, M. *Angew. Chem.* **2008**, *120*, 2926-2929.
(41) Hassanpour, S.; Taghizadeh, M.; Yaripour, F. *Ind. Eng. Chem. Res.* **2010**, *49*, 4063-4069.
(42) Jimenez, I.; Centeno, M. A.; Scotti, R.; Morazzoni, F.; Arbiol, J.; Cornet, A.; Morante, J. R. *J. Mater. Chem.* **2004**, *14*, 2412-2420.
(43) Chen, J.; Thomas, J. M. *J. Chem. Soc., Chem. Commun.* **1994**, 603-604.
(44) Vermaire, D. C.; van Berge, P. C. *J. Catal.* **1989**, *116*, 309-317.
(45) Guo, Y.; Gu, D.; Jin, Z.; Du, P.-P.; Si, R.; Tao, J.; Xu, W.-Q.; Huang, Y.-Y.; Senanayake, S.; Song, Q.-S.; Jia, C.-J.; Schuth, F. *Nanoscale* **2015**, *7*, 4920-4928.
(46) Wittstock, A.; Zielasek, V.; Biener, J.; Friend, C. M.; Bäumer, M. *Science* **2010**, *327*, 319-322.
(47) Xu, B.; Liu, X.; Haubrich, J.; Madix, R. J.; Friend, C. M. *Angew. Chem. Int. Ed.* **2009**, *48*, 4206-4209.

(48) Behera, G. C.; Parida, K.; Dummer, N. F.; Whiting, G.; Sahu, N.; Carley, A. F.; Conte, M.; Hutchings, G. J.; Bartley, J. K. *Catal. Sci. Technol.* **2013**, *3*, 1558-1564.
(49) Li, W.; Liu, H.; Iglesia, E. *J. Phys. Chem. B* **2006**, *110*, 23337-23342.
(50) Liu, H.; Iglesia, E. *J. Phys. Chem. B* **2005**, *109*, 2155-2163.
(51) Centi, G.; Golinelli, G.; Busca, G. *J. Phys. Chem.* **1990**, *94*, 6813-6819.
(52) Guliants, V. V.; Benziger, J. B.; Sundaresan, S.; Wachs, I. E.; Jehng, J. M.; Roberts, J. E. *Catal. Today* **1996**, *28*, 275-295.

Table of Contents Graphic